Asian Journal of Chemistry; Vol. 37, No. 7 (2025), 1655-1665

ASIAN JOURNAL OF CHEMISTRY

https://doi.org/10.14233/ajchem.2025.33896

Structural, Theoretical and Molecular Docking Evaluation of 2-Methyl-1,4-naphthoquinone as Potential Anti-Breast Cancer Agent

J. SENTHIL KUMAR[1], N. SIVA JYOTHI[2], S. SUMATHI[3], N. KARTHIK[3], K. VINOTH[4] and S. JEYAVIJAYAN[3,*]

[1]PG & Research Department of Physics, Thanthai Periyar Government Arts and Science College, Tiruchirappalli-620023, India
[2]Department of Physics, Periyar Maniammai Institute of Science and Technology, Vallam, Thanjavur-613403, India
[3]Department of Physics, Kalasalingam Academy of Research and Education, Krishnankoil-626126, India
[4]Department of Physics, J.J. College of Engineering and Technology, Tiruchirappalli-620009, India

*Corresponding author: E-mail: sjeyavijayan@gmail.com

Received: 19 April 2025; *Accepted*: 6 June 2025; *Published online*: 30 June 2025; AJC-22040

The DFT-B3LYP/6-311++G(d,p) method was employed to investigate the vibrational characteristics of 2-methyl-1,4-naphthoquinone (2MNQ), with results compared against FTIR and FT-Raman spectra recorded in the 3500–400 cm^{-1} range. The optimized molecular geometry was validated through comparison with both theoretical predictions and experimental X-ray diffraction (XRD) data. Charge density distributions were analyzed to elucidate the energy gap between the highest occupied molecular orbital (HOMO) and the lowest unoccupied molecular orbital (LUMO) and to construct the molecular electrostatic potential (MEP) map, offering insights into the potential biological activity of compound. Electronic absorption spectra were simulated using time-dependent density functional theory (TD-DFT) with the same basis set. Mulliken charge analysis highlighted significant electron delocalization, supporting the electronic reactivity of molecule. Moreover, the density of states (DOS) spectrum was examined to identify key molecular orbital contributions. Molecular docking studies revealed that 2MNQ exhibited the highest binding affinity with the breast cancer-related protein 1M17, showing a binding energy of –7.2 kcal/mol. ADMET predictions further assessed the drug-likeness and pharmacokinetic properties of the compound. These combined theoretical and experimental findings provide valuable insights into the molecular structure and potential pharmacological applications of 2MNQ.

Keywords: 2-Methyl-1,4-naphthoquinone, DFT, Molecular docking, Breast cancer, ADMET.

INTRODUCTION

Breast cancer remains one of the most common and life-threatening diseases worldwide, with increasing incidence and mortality rates. Despite advancements in conventional treatments such as surgery, chemotherapy and targeted therapies, drug resistance and adverse side effects continue to present significant challenges [1]. Consequently, the search for novel, more effective and safer therapeutic agents is a critical area of research [2]. Naphthoquinone derivatives, a class of naturally occurring and synthetic compounds, have attracted considerable attention due to their potent anticancer properties. These compounds are characterized by a quinone core structure, which plays a crucial role in various biological activities, including the modulation of oxidative stress, induction of apoptosis and arrest of the cell cycle [3]. Many naturally derived naphthoquinones, such as lawsone, plumbagin and shikonin, have demonstrated strong cytotoxic effects against various cancer cell lines, including breast cancer [4].

The anticancer mechanisms of naphthoquinone derivatives involve multiple pathways, including the generation of reactive oxygen species (ROS), inhibition of topoisomerases, modulation of key signaling pathways and interactions with tumor suppressor proteins [5]. Their ability to target multiple cellular processes makes them promising candidates for breast cancer therapy, either as standalone agents or in combination with existing chemotherapeutic drugs [6]. This study explores the potential of naphthoquinone derivatives in breast cancer treatment, discussing their mechanisms of action, structure–activity relationships and preclinical studies [7]. Understanding their therapeutic potential could pave the way for the development of new, more effective breast cancer treatments with reduced toxicity and improved patient outcomes [8].

According to current literature, researchers have investigated the DFT (density functional theory) studies of various naphthoquinone derivatives [9]. Furthermore, several studies have examined their anticancer potential [10]. The application of DFT calculations to better understand the structural and vibrational characteristics of molecules has become increasingly important in the pharmaceutical industry. However, no quantum chemistry calculations or molecular docking investigations of 2-methyl-1,4-naphthoquinone (2MNQ) have been reported in the literature to date. In this context, DFT calculations, in combination with vibrational spectroscopy, have for the first time revealed structural and quantum chemical data for 2MNQ [11].

In this work, molecular stability and characterization were investigated using a combination of X-ray diffraction (XRD), infrared, Raman and ultraviolet–visible (UV–vis) spectroscopy techniques. The extremely low energy state of 2MNQ molecule was further confirmed through DFT optimization. Using the DFT/6-311++G(d,p) basis set, extensive theoretical calculations were carried out to optimize geometrical parameters, evaluate the HOMO–LUMO energy gap, calculate Mulliken charges analyze and the molecular electrostatic potential (MEP). The density of states (DOS) spectrum was employed to characterize each frontier molecular orbital and to compute key quantum chemical descriptors, including electronegativity, hardness, chemical softness and the electrophilicity index of 2MNQ. Docking analysis was performed to investigate the pharmacological potential of 2MNQ and its interactions with breast cancer related drug targets. The ADMET (absorption, distribution, metabolism, excretion and toxicity) properties were also evaluated to assess its drug-likeness. Overall, this study presents a comprehensive examination of the biological, vibrational and electronic properties of 2MNQ, supported by both theoretical and experimental data.

EXPERIMENTAL

Characterization: The 2MNQ compound was used without any further purification after being acquired from Sigma-Aldrich, USA. Structural information about the compound was investigated in the 2θ range of 10º-50º using a Bruker-D8 X-ray diffractometer. The FTIR spectrum of the molecule (3500-400 cm^{-1}) was recorded using a Perkin-Elmer FTIR spectrometer equipped with a globar source, a KBr beam splitter, an MCT detector and a spectral resolution of ± 1 cm^{-1}. The FT-Raman spectrum of 2MNQ was obtained using a computer-interfaced Bruker IFS 66V interferometer equipped with FRA-106 FT-Raman accessories. The spectrum was recorded at a scanning speed of 10 cm^{-1} and a spectral resolution of 2 cm^{-1} at ambient temperature. UV–visible spectra were acquired using a U-3501 spectrophotometer.

Computational details: All quantum chemical calculations for 2MNQ molecule were performed at the DFT/B3LYP level of theory [12,13], using the Gaussian 09W program suite [14] without imposing any geometric constraints. The 6-311++G(d,p) basis set was employed for all computations. Vibrational frequencies were calculated using the VEDA program [15] and scaled by a factor of 0.961 [16]. Moreover, frontier molecular orbitals (FMO), molecular electrostatic potential (MEP) and Mulliken charges were computed at the same theoretical level by integrating the results from the GaussView program [17].

Molecular docking studies: Multiple downstream cellular signaling pathways activated by human progesterone and estrogen receptors contribute to the development and progression of cancer. A computer-aided molecular modeling approach was employed to evaluate the inhibitory potential of 2MNQ against breast cancer. Epidermal growth factor (PDB ID: 1M17), estrogen receptor (PDB ID: 1A52) and human progesterone receptor (PDB ID: 3D90) were selected as protein markers for breast cancer. These receptors served both as protein indicators and as ligands for the chemical compound 2MNQ. The PyRx molecular graphics toolkit [18] and AutoDock Vina [19] were used to visualize the protein-ligand binding sites. Discovery Studio [20] was utilized to analyze the protein structures and identify the positions of amino acids.

ADMET prediction: The pharmacokinetic and physicochemical properties of the drug 2MNQ were determined using the pkCSM server [21]. The BOILED-Egg model was subsequently applied *via* the SwissADME web server, which predicted various pharmacokinetic characteristics, including drug-likeness and water solubility [22]. The chemical structure of 2MNQ was used to evaluate a range of physico-chemical and pharmacokinetic parameters, such as absorption, aqueous solubility, distribution, metabolism, excretion and toxicity.

RESULTS AND DISCUSSION

Geometrical parameters: The monoclinic space group $P2_1/a$ is the crystallographic setting in which 2MNQ crystallizes, as determined by XRD data [23]. The unit cell parameters are a = 11.13247(12) Å, b = 20.67256(17) Å, c = 7.44834(5) Å and β = 97.9850(6)º. Fig. 1 shows the powder X-ray diffraction (XRD) pattern of the synthesized 2MNQ alongside the standard pattern generated from the Crystallographic Information File (CIF). The strong correlation between these two patterns confirms the structural integrity of the molecule. The mole-cular structure of 2MNQ exhibits C_1 point group symmetry. Using the DFT-B3LYP method with the 6-311++G(d,p) basis set, the optimized structural parameters were determined according to the atom numbering scheme shown in Fig. 2. As presented in Table-1, theoretical values were compared with the experimental data [23]. The root mean square deviation (RMSD) was used to evaluate the agreement between the theoretical and experimental structures, yielding R^2 = 0.8969 for bond angles and R^2 = 0.9913 for bond lengths. Structurally, 2MNQ consists of two C–O bonds, twelve C–C bonds and seven C–H bonds. The lengths of the C–H bonds range from 1.08 to 1.09 Å. Based on B3LYP/6-311++G(d,p) calculations, the experimental C–C bond distances (1.37–1.50 Å) increase slightly in the theoretical results (1.39–1.50 Å). Notable bond angles that closely match their experimental counterparts include C2–C1–C6 at 118.2º (119.0º by expt.), C3–C4–O11 at 120.6º (121.0º by expt.) and C6–C7–H21 at 118.7º (120.0º by expt.).

Fig. 3 displays the correlation coefficient plot, which shows the strong agreement between the estimated and experimental parameters. To study the thermodynamic characteristics of

TABLE-1
OPTIMIZED STRUCTURAL PARAMETERS OF 2-METHYL-1,4-NAPHTHOQUINONE

Bond length (Å)	DFT-B3LYP/6-311++G(d,p)	Experimental [Ref. 23]	Bond angle (°)	DFT-B3LYP/6-311++G(d,p)	Experimental [Ref. 23]	Bond angle (°)	DFT-B3LYP/6-311++G(d,p)	Experimental [Ref. 23]
C1-C2	1.50	1.47	C2-C1-C6	118.2	119.0	C6-C7-C8	120.0	119.7
C1-C6	1.49	1.47	C2-C1-O12	120.1	121.1	C6-C7-H21	118.7	120.0
C1-O12	1.22	1.23	C6-C1-O12	121.7	120.0	C8-C7-H21	121.3	120.4
C2-C3	1.35	1.38	C1-C2-C3	119.9	120.0	C7-C8-C9	120.2	120.0
C2-C13	1.50	1.49	C1-C2-C13	116.6	118.8	C7-C8-H20	119.9	119.7
C3-C4	1.48	1.50	C3-C2-C13	123.5	120.2	C9-C8-H20	120.0	120.3
C3-H17	1.09	1.08	C2-C3-C4	123.7	120.8	C8-C9-C10	120.2	120.0
C4-C5	1.49	1.47	C2-C3-H17	121.4	119.4	C8-C9-H19	120.0	119.7
C4-O11	1.22	1.24	C4-C3-H17	114.9	119.7	C10-C9-H19	119.9	119.7
C5-C6	1.40	1.41	C3-C4-C5	117.4	118.0	C5-C10-C9	120.0	119.3
C5-C10	1.40	1.38	C3-C4-O11	120.6	121.0	C5-C10-H18	118.6	120.1
C6-C7	1.40	1.39	C5-C4-O11	122.0	121.0	C9-C10-H18	121.4	120.5
C7-C8	1.39	1.37	C4-C5-C6	120.1	120.4	C2-C13-H14	111.1	109.4
C7-H21	1.08	1.08	C4-C5-C10	120.0	120.2	C2-C13-H15	110.5	109.0
C8-C9	1.40	1.41	C6-C5-C10	119.9	119.4	C2-C13-H16	110.5	109.8
C8-H20	1.08	1.09	C1-C6-C5	120.7	120.8	H14-C13-H15	109.2	108.0
C9-C10	1.39	1.40	C1-C6-C7	119.5	118.2	H14-C13-H16	109.2	108.0
C9-H19	1.08	1.08	C5-C6-C7	119.8	121.0	H15-C13-H16	106.1	105.0
C10-H18	1.08	1.08						
C13-H14	1.09	1.07						
C13-H15	1.09	1.08						
C13-H16	1.09	1.08						

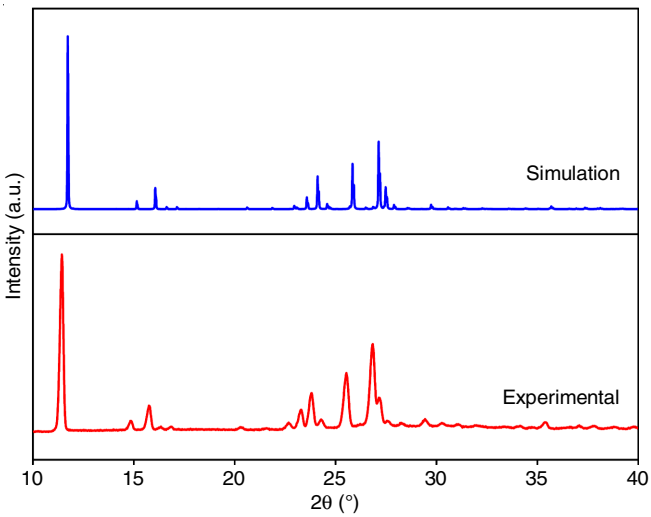

Fig. 1. Simulated XRD of 2-methyl-1,4-naphthoquinone compared with experimental X-ray diffraction pattern

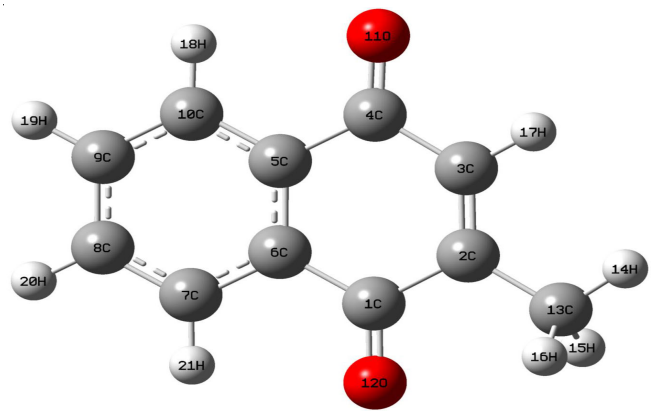

Fig. 2. Optimized structure of 2-methyl-1,4-naphthoquinone

2MNQ, the DFT/B3LYP method with the 6-311++G(d,p) basis set was employed and the results are summarized in Table-2. Due to the presence of strongly electronegative nitrogen and bromine atoms, 2MNQ exhibits a relatively high dipole moment of 1.1194 Debye. The molecule was found to have entropy of 100.162 cal mol^{-1} K^{-1} and a total energy of 106.683 kcal mol^{-1}. The zero-point vibrational energy was calculated to be 100.148 kcal mol^{-1}. These thermodynamic properties provide valuable insights for evaluating the chemical reactivity and potential applications of 2MNQ.

TABLE-2
THERMODYNAMIC PARAMETERS OF 2-METHYL-1,4-NAPHTHOQUINONE (2MNQ)

Parameters	DFT-B3LYP/6-311++G(d,p)
Optimized global minimum energy (Hartrees)	-574.59068
Total energy (thermal), E_{total} (kcal mol^{-1})	106.683
Heat capacity, C_v (cal mol^{-1} k^{-1})	40.428
Total entropy, S (cal mol^{-1} k^{-1})	100.162
Translational entropy (cal mol^{-1} k^{-1})	41.336
Rotational entropy (cal mol^{-1} k^{-1})	30.888
Vibrational entropy (cal mol^{-1} k^{-1})	27.939
Vibrational energy, E_{vib} (kcal mol^{-1})	104.905
Zero-point vibrational energy (kcal mol^{-1})	100.148
Rotational constants (GHz)	
A	1.28793
B	0.76837
C	0.48267
Dipole moment (Debye)	1.1194

Vibrational assignment: The vibrational modes of 2MNQ, which are active in both infrared and Raman spectra, are governed by its 21 constituent atoms. The experimental and computational spectra of 2MNQ are presented in Fig. 4, while the

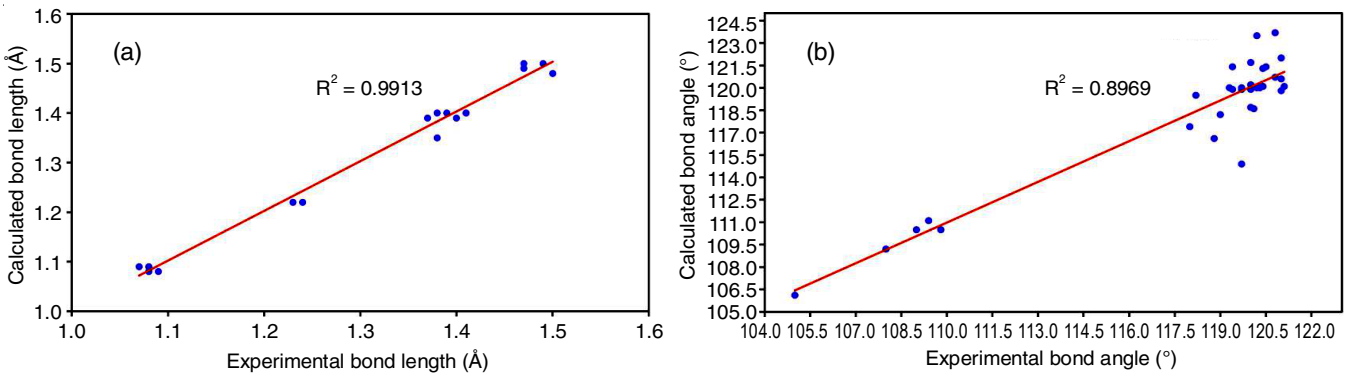

Fig. 3. Correlation graphs of the calculated and experimental molecule (a) bond distances and (b) bond angles of 2-methyl-1,4-naphthoquinone

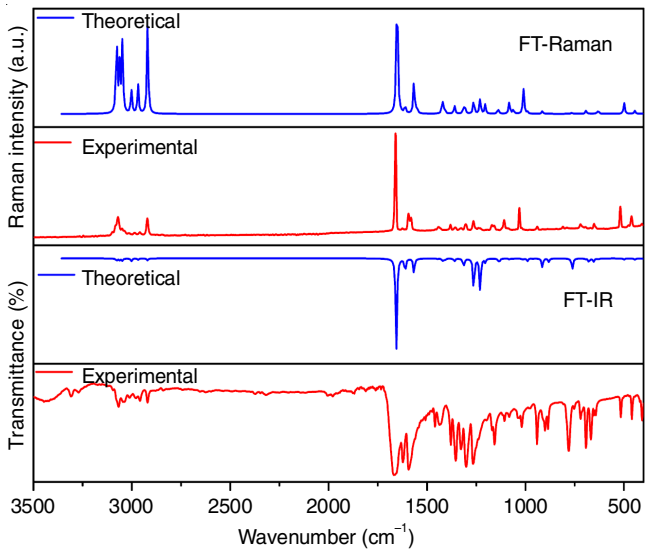

Fig. 4. FTIR and FT-Raman spectrum of 2-methyl-1,4-naphthoquinone

fundamental vibrational modes are listed in Table-3. The primary objective of this study is to accurately assign the experimental frequencies to the corresponding vibrational modes of 2MNQ, in alignment with the harmonic vibrational frequencies predicted by density functional theory (DFT). A comparison between the experimental results and the frequencies calculated using the DFT-B3LYP method [12] reveals a systematic overestimation of vibrational modes, which can be attributed to the absence of anharmonic effects in the theoretical model.

The vibrational analysis of each CH_3 group in 2MNQ includes nine fundamental modes: symmetrical stretching, in-plane and out-of-plane stretching, in-plane bending, symmetrical and asymmetrical deformation, in-plane and out-of-plane rocking and twisting ($\tau(CH_3)$) modes. Frequencies were assigned to these modes accordingly [24]. Asymmetric stretching vibrations are observed in the 3010–2970 cm^{-1} range, while symmetric stretching vibrations appear between 2990 and 2940 cm^{-1}. The FTIR and Raman spectra of 2MNQ reveal characteristic vibrational modes associated with the CH_3 group. The in-plane stretching and CH_3 symmetric stretching frequencies appear at 3016 cm^{-1} (infrared), 2998 cm^{-1} (Raman), 2978 cm^{-1} (infrared), 2957 cm^{-1} (Raman), respectively. CH_3 symmetric bending is observed at 1350 cm^{-1}, while in-plane bending modes are evident at 1435 cm^{-1}. Furthermore, CH_3 in-plane and out-of-plane rocking modes contribute to infrared bands at 1017 cm^{-1} and 775 cm^{-1}, respectively. Out-of-plane stretching and bending modes are reflected in the infrared spectrum at 1154 cm^{-1} and 2971 cm^{-1} (FTIR), as well as at 2919 cm^{-1} (Raman). The remaining vibrational modes of the CH_3 group are summarized in Table-3. These spectral assignments are further supported by the literature and show strong agreement with previously reported values [24].

Many of the weak bands typically observed in the 3100–3000 cm^{-1} region of aromatic compounds are attributed to C–H stretching vibrations [25]. In case of 2MNQ, C–H stretching vibrations are identified in the Raman bands at 3076 and 3049 cm^{-1} as well as in the infrared bands at 3071, 3069 and 3039 cm^{-1}. These vibrations are confirmed based on their potential energy distribution (PED) values. Sharp bands in the 1300–1000 cm^{-1} range correspond to C–C stretching vibrations and are associated with C–H in-plane ring bending. In 2MNQ, C–H in-plane bending vibrations are represented by FT-IR bands at 1085 and 1005 cm^{-1} and FT-Raman bands at 1115 and 1053 cm^{-1}. The theoretically predicted C–H vibrational modes, calculated using the B3LYP/6-311++G(d,p) method, show excellent agreement with the experimental observations.

The C=O stretching vibration typically appears in the 1700–1600 cm^{-1} range [26]. In case of 2MNQ, the scaled C=O stretching frequencies are 1658 cm^{-1} in FTIR (with 92% PED) and 1651 cm^{-1} in Raman (with 91% PED). Conjugation can enhance the intensity of C=O bands, making them easier to identify. In 2MNQ, the vibrational bands corresponding to C=O in-plane and out-of-plane bending modes are presented in Table-3. These frequency assignments are further supported by the literature [26].

The C–C stretching vibrations, typically observed in the 1625–1200 cm^{-1} range, are significant for substituted aromatic compounds [27]. In 2MNQ, the C–C stretching modes corresponding to experimental peaks exhibit PED values between 81% and 90%. These vibrations are observed in the infrared spectrum at 1620, 1576, 1543, 1461, 1400, 1320, 1306, 1268, 1237 and 1200 cm^{-1} and in the Raman spectrum at 1599, 1580, 1433, 1306, 1268 and 1238 cm^{-1}. In addition to these stretching modes, the in-plane and out-of-plane bending vibrations for each normal mode have been calculated based on literature data [27] and are listed in Table-3.

UV-vis analysis: The absorption characteristics of the molecular system were investigated using time-dependent

TABLE-3
VIBRATIONAL ASSIGNMENTS BASED ON PED CALCULATIONS FOR 2-METHYL-1,4-NAPHTHOQUINONE

S. No.	Observed wavenumber (cm^{-1})		Wavenumber (cm^{-1})		IR intensity (Km mol^{-1})	Raman activity (Å^4 amu^{-1})	Assignment with PED (%)
	FT-IR	FT- Raman	Calculated	Scaled			
1	–	3076(ms)	3202	3078	10	220	νCH (100)
2	3070(w)	–	3198	3075	1	30	νCH (99)
3	3069(w)	–	3185	3062	8	140	νCH (96)
4	–	3049(vw)	3171	3048	3	74	νCH (99)
5	3039(w)	–	3170	3048	7	138	νCH (96)
6	3016(vw)	2998(vw)	3123	3002	12	70	CH_3ips (95)
7	2978(vw)	2957(vw)	3088	2968	6	87	CH_3ss (94)
8	2917(w)	2919(ms)	3037	2920	8	261	CH_3ops (93)
9	1658(vs)	–	1723	1656	387	5	νC=O (92)
10	–	1651(vs)	1719	1652	37	318	νC=O (91)
11	1620(s)	1599(ms)	1676	1611	63	17	νCC (90)
12	1576(vs)	1580(w)	1629	1566	70	72	νCC (89)
13	1543(vw)	–	1614	1551	1	11	νCC (91)
14	1461(w)	–	1506	1448	2	1	νCC (90)
15	–	1433(vw)	1484	1426	0	3	νCC (88)
16	1435(w)	–	1479	1421	10	25	CH_3ipb (87)
17	1400(w)	–	1467	1410	9	9	νCC (86)
18	1350(ms)	1359(vw)	1416	1361	13	17	CH_3sb (85)
19	1320(ms)	–	1367	1315	38	14	νCC (87)
20	1306(ms)	1306(vw)	1358	1305	2	9	νCC (84)
21	1268(ms)	1268(vw)	1314	1263	155	28	νCC (83)
22	1237(vw)	1238(vw)	1280	1230	150	30	νCC (82)
23	1200(vw)	–	1253	1204	16	17	νCC (81)
24	1154(w)	–	1186	1140	4	9	CH_3opb (80)
25	–	1115(w)	1179	1134	16	1	βCH (81)
26	1085(vw)	–	1125	1082	4	23	βCH (79)
27	–	1053(ms)	1104	1061	2	8	βCH (78)
28	1017(w)	–	1058	1017	3	0	CH_3ipr (77)
29	1005(vw)	–	1050	1010	3	45	βCH (76)
30	985(vw)	–	1030	990	12	3	βCH (75)
31	979(vw)	–	1020	980	0	0	Rasymd (74)
32	–	952(vw)	1002	963	1	0	Rsymd (75)
33	931(ms)	–	951	914	40	5	Rtrigd (73)
34	895(ms)	–	917	882	11	0	Rasymd (72)
35	879(w)	–	916	880	4	0	Rsymd (71)
36	–	785(vw)	802	771	1	0	Rtrigd (70)
37	775(w)	–	797	767	7	1	CH_3opr (69)
38	749(ms)	–	792	761	43	1	βCC (68)
39	–	691(vw)	720	692	3	5	τRasymd (67)
40	682(ms)	–	705	677	17	0	τRsymd (66)
41	665(ms)	653(vw)	680	654	15	0	τRtrigd (65)
42	643(vw)	–	660	635	2	4	τRasymd (66)
43	630(vw)	–	652	627	2	3	τRsymd (64)
44	521(w)	521(w)	519	499	5	18	τRtrigd (62)
45	–	–	480	461	0	0	τRasymd (63)
46	452(mw)	450(ms)	462	445	5	5	ωCH (61)
47	407(ms)	412(vw)	426	410	0	0	ωCH (60)
48	–	–	407	392	10	2	ωCH (61)
49	–	–	300	289	12	2	ωCC(59)
50	–	–	355	341	0	0	βC=O (58)
51	–	–	379	365	0	2	βC=O (57)
52	–	–	253	243	1	2	ωCH (56)
53	–	–	206	198	0	1	ωCH (57)
54	–	–	159	153	1	2	ωC=O (55)
55	–	–	127	122	0	0	ωC=O (54)
56	–	–	120	115	0	1	τCH_3 (55)
57	–	–	58	56	9	0	Butterfly (53)

density functional theory (TD-DFT) [28]. Electronic absorption spectra of 2MNQ in the gas phase were simulated using the B3LYP/6-311++G(d,p) basis set. The UV-Vis spectra of 2MNQ are shown in Fig. 5a. An absorption peak corresponding to a π→π* transition, primarily involving a HOMO–2 to LUMO excitation with a 93.53% contribution, is observed at 342.57 nm. The predicted absorption wavelengths, oscillator strengths and excitation energies [29] are summarized in Table-4. Moreover, the calculated spectra display absorption peaks at 352.47 nm, with associated excitation energies of 3.5176 eV.

Frontier molecular orbitals (FMOs): The electrical properties, chemical reactivity and molecular transitions of 2MNQ were evaluated using frontier molecular orbital (FMO) analysis. FMO analysis also provides insight into the characteristics of ligand molecules and their interactions with biological receptors [30]. The highest occupied molecular orbital (HOMO) represents the ability to donate electrons of molecule, while the lowest unoccupied molecular orbital (LUMO) reflects its capacity to accept electrons. In 2MNQ, the HOMO energy (E_{HOMO}) was calculated as –7.46 eV and the LUMO energy (E_{LUMO}) as –3.42 eV, resulting in an energy gap (ΔE) of 4.04 eV, indicating a stable molecular structure. The FMOs of 2MNQ are illustrated in Fig. 5b. The LUMO is primarily localized on the naphthoquinone ring moiety, while the HOMO is concentrated around the oxygen atoms and methyl group. In the visual representation, red and green correspond to the positive and negative phases of the FMO, respectively. The energy gap further supports the stability and low chemical reactivity of molecule. Koopman's theorem [31] was applied to determine several molecular descriptors related to FMOs, which are listed in Table-5. These include ionization potential, electron affinity, chemical potential, hardness (η), softness (S) and electrophilicity index (ω). In 2MNQ, the electronegativity (χ), representing the molecule's tendency to attract electrons, was calculated to be 5.44 eV. The molecule exhibited a hardness of 2.02 eV and a softness of 0.25 eV^{-1}, indicating moderate chemical reactivity. According to Domingo *et al.* [32], the electrophilicity scale, organic compounds are categorized as weak electrophiles (ω

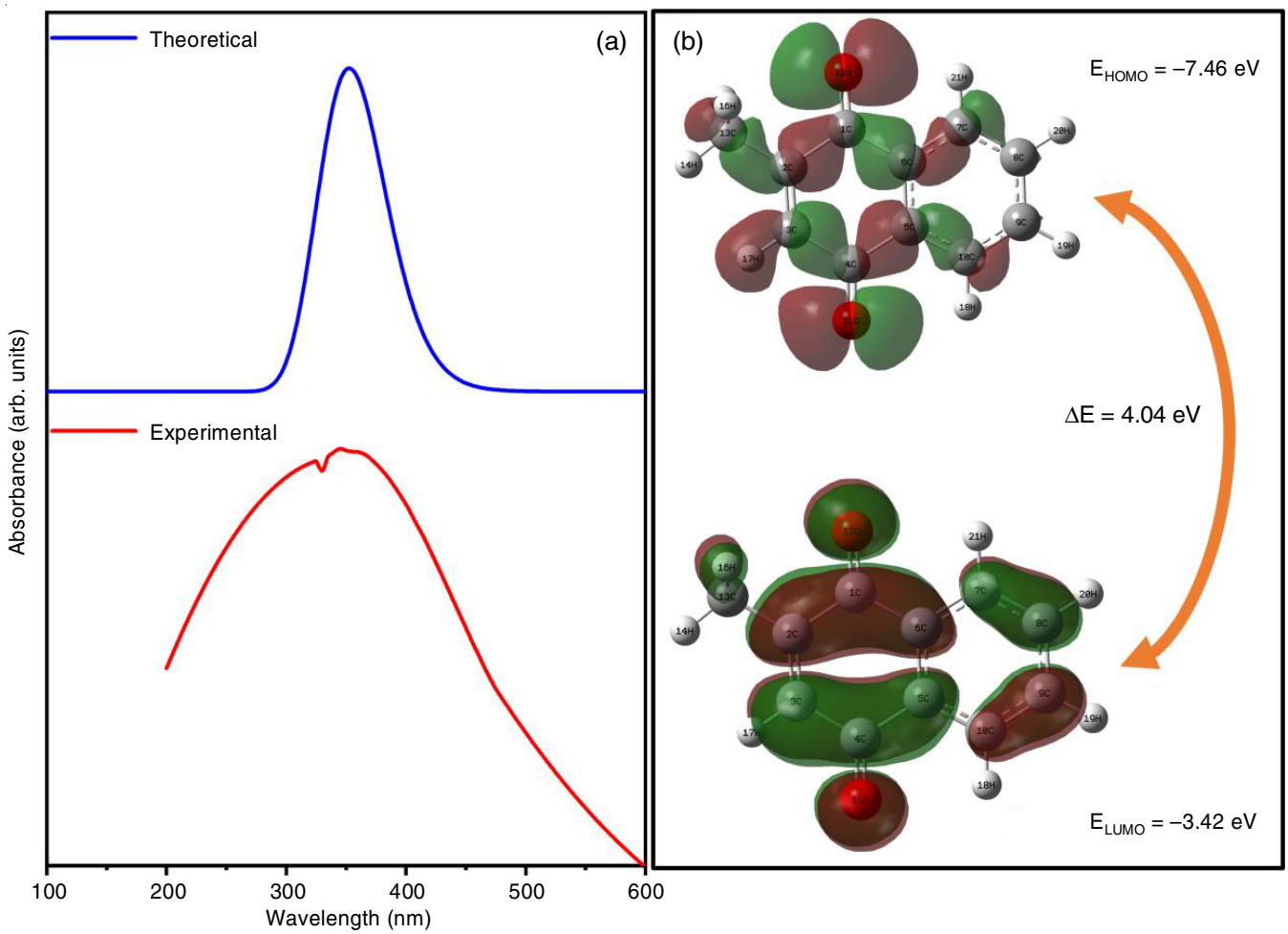

Fig. 5. (a) UV-vis spectra and (b) HOMO-LUMO of 2-methyl-1,4-naphthoquinone

TABLE-4
MOLECULAR ORBITAL CONTRIBUTIONS OF 2-METHYL-1,4-NAPHTHOQUINONE

TD-DFT/B3LYP/6-311++G(d,p)					Experimental wavelength (nm)
Energy (eV)	Oscillator strength	Computed wavelength (nm)	Major contributions	Assignment	
3.5176	0.0016	352.47	H-2 to L (93.53%)	π→π*	342.57

TABLE-5
GLOBAL REACTIVITY DESCRIPTORS FOR
2-METHYL-1,4-NAPHTHOQUINONE

Molecular properties	B3LYP/6-311++G(d,p)
HOMO (eV)	-7.46
LUMO (eV)	-3.42
ΔE ($E_{HOMO} - E_{LUMO}$) (eV)	4.04
Ionization potential (I) (eV)	7.46
Electron affinity (A) (eV)	3.42
Global hardness (η) (eV)	2.02
Global softness (S) (eV^{-1})	0.25
Electronegativity (χ) (eV)	5.44
Chemical potential (μ) (eV)	-5.44
Global electrophilicity (ω) (eV)	7.31

< 0.8 eV), moderate electrophiles (0.8 < ω < 1.5 eV), or strong electrophiles (ω > 1.5 eV). With an electrophilicity index of 7.31 eV, 2MNQ is classified as a strong electrophile.

In regions, where the molecular orbitals have nearly degenerate energy levels, describing electronic behaviour using only HOMO and LUMO may be insufficient. The density of states (DOS) analysis provides a more detailed perspective. Using GaussSum 3.0, DOS was calculated by summing the alpha (α) and beta (β) electron densities, incorporating Gaussian-curved molecular orbital data [33]. For 2MNQ, the total DOS includes 90 electrons, consisting of 45 α and 45 β electrons. As shown in Fig. 6, the distribution of molecular orbitals plays a critical role in defining the chemical bonding and electronic characteristics of the molecule.

Molecular electrostatic potential & Mulliken charge: In Fig. 7a, a molecular electrostatic potential (MEP) map is projected onto the molecule's van der Waals surface. On this multicoloured surface, regions of high electron density (negative potential) are represented by red areas (oxygen atoms in 2MNQ), while regions of low electron density (positive potential) are shown in blue (hydrogen atoms in 2MNQ). This MEP mapping helps in identifying the reactive sites of molecule and predicting the potential interactions with electrophiles and

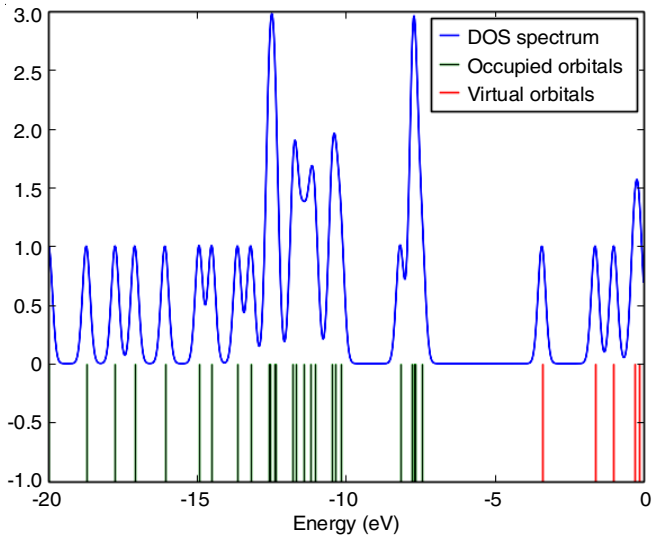

Fig. 6. DOS spectrum of 2-methyl-1,4-naphthoquinone

nucleophiles [34]. The MEP surface also provides insights into the charge distribution across the molecular framework, suggesting that the molecule is an aromatic compound with various substituents.

This is further supported by Fig. 7b, which presents a 3D model of the molecule, with each atom's atomic charge clearly labeled in parentheses. The colour of the atoms reflects the sign and magnitude of their atomic charges: black indicates near-neutral atoms, green represents positively charged atoms and red denotes highly negative regions. The numerical charges help quantify local electron-rich and electron-deficient zones, reinforcing the qualitative insights derived from the MEP mapping in Fig. 7a. Together, these two visualizations offer a comprehensive representation of the electronic structure of molecule and are instrumental in identifying potential sites of intermolecular interactions and chemical reactivity [35]. The Mulliken charge distribution provides critical insight into the electronic characteristics of atoms within the 2MNQ molecule.

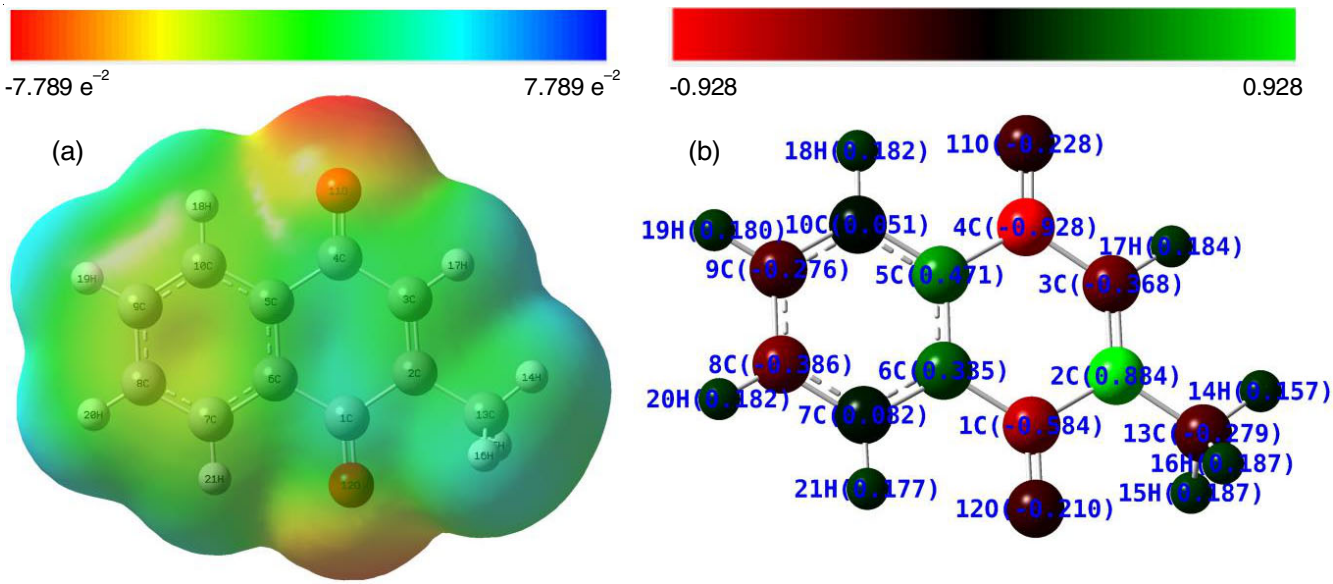

Fig. 7. (a) MEP plot of 2-methyl-1,4-naphthoquinone (b) Mulliken population analysis of 2-methyl-1,4-naphthoquinone

Atoms such as C4 (–0.93), C1 (–0.58) and O11 (–0.23) carry substantial negative charges, suggesting strong nucleophilic behaviour shown in Table-6. These findings are consistent with the red, electron-rich regions observed in the MEP map. Conversely, the electrophilic nature of hydrogen atoms H14–H16 is confirmed by their high positive Mulliken charges (0.16–0.19), which correspond to the electron-deficient blue areas in the MEP visualization. In combination, the Mulliken charge analysis and MEP mapping effectively highlight the electron density distribution, helping in the prediction of chemically reactive sites within the 2MNQ molecule.

TABLE-6
MULLIKEN ATOMIC CHARGE FOR
2-METHYL-1,4-NAPHTHOQUINONE

Atoms	Atomic charges (Mulliken) by B3LYP/6-311++G(d,p)	Atoms	Atomic Charges (Mulliken) by B3LYP/6-311++G(d,p)
C1	-0.58	O12	-0.21
C2	0.88	C13	-0.28
C3	-0.37	H14	0.16
C4	-0.93	H15	0.19
C5	0.47	H16	0.19
C6	0.34	H17	0.18
C7	0.08	H18	0.18
C8	-0.39	H19	0.18
C9	-0.28	H20	0.18
C10	0.05	H21	0.18
O11	-0.23		

Molecular docking: In pharmacological drug research, molecular docking is a widely used technique for investigating the binding sites between proteins and ligands. Based on previous studies, human progesterone and estrogen receptors were selected for present analysis. *in silico* study (Fig. 8) illustrates the interactions between 2MNQ and several proteins associated with breast cancer, including the human progesterone receptor (PDB ID: 1M17), epidermal growth factor, human estrogen receptor (PDB ID: 1A52) and estrogen sulfotransferase (PDB ID: 3D9O). As shown in Table-7, 2MNQ exhibits the highest binding affinity with the 1M17 protein, with a binding energy of –7.2 kcal/mol. However, only one hydrogen bond interaction was observed in this complex. The hydrogen bond distance between the interacting residue, ASP A:831 and the ligand is approximately 3.80 Å.

As shown in Fig. 8b, this study indicates that 2MNQ interacts with the 1A52 receptor with a binding energy of –7.1 kcal/mol, forming a single conventional hydrogen bond. The interaction involves the HIS A:524 residue, with a bond distance of 2.72 Å. Additionally, 2MNQ forms a single hydrogen bond with the 3D9O receptor *via* the SER A:728 residue, with a separation of 2.76 Å, as illustrated in Fig. 8c. The 3D9O protein also exhibits a significant binding affinity (–6.6 kcal/mol) for 2MNQ. These interactions suggest that the 2MNQ ligand binds effectively to proteins associated with breast cancer, potentially impairing their biological function.

ADMET prediction: The absorption and metabolic properties of 2MNQ are presented in Table-8. A log Papp value greater than 0.90, as reported by the pkCSM server, indicates high Caco-2 permeability. Since, the intestine plays a crucial role in the absorption of food and drugs, a compound is considered to have poor human intestinal absorption (HIA) if its absorption rate is below 30% [36]. In case of 2MNQ, 97.779% is absorbed in the human intestine, suggesting excellent oral bioavailability. One of the main challenges in topical drug development is overcoming the protective barrier of skin. Several *in silico* approaches were used to predict 2MNQ's skin penetration. According to the pkCSM server, 2MNQ has a skin permeability (log Kp) of –2.346, indicating significant dermal absorption. The volume of distribution at steady state (VDss) reflects the extent to which a drug spreads throughout body tissues relative to the plasma. A higher VDss suggests wider tissue distribution. For 2MNQ, the VDss (log L/kg) was calculated to be 0.094, indicating a reasonable degree of distribution. The blood–brain barrier (BBB) plays a key role in protecting the brain from harmful substances. A log BB value greater than 0.3 indicates good permeability across the BBB, while a value below -1 implies poor distribution to the brain. 2MNQ recorded a log BB value of 0.408, suggesting effective brain penetration. CNS permeability (log PS), assessed through direct carotid artery injection, provides another metric. Compounds with log PS < -3 are predicted to have poor CNS penetration, whereas those with log PS > -2 are expected to penetrate the CNS. 2MNQ's log PS of -2.004 implies that it is likely capable of crossing into the CNS. Regarding renal clearance, the pkCSM server reports a total clearance rate of 0.223 for 2MNQ, when used as a renal OCT2 substrate. In terms of toxicity, the LOAEL and oral LD_{50} in rats were found to be 2.657 mol/kg and 1.696 log mg/kg bw/day, respectively. Notably, 2MNQ does not inhibit hERG I or II, according to pkCSM predictions, which is favourable for cardiac safety.

The BOILED-Egg model was used to evaluate passive gastrointestinal absorption and brain penetration, with results displayed in Fig. 9. P-glycoprotein (P-gp) plays a key role in drug transport through the intestinal, renal and hepatic systems and is known to affect drug bioavailability and excretion [37]. The model shows that 2MNQ is located in the yolk region (Fig. 9a), indicating its capability to cross the blood–brain barrier. Among the drug-likeness rules assessed, 2MNQ violated only the Ghose rule, due to its molecular weight of 172.18 g/mol. The saturation level of compound, evaluated using the fraction of sp^3 hybridized carbon atoms (Csp^3), was found to

TABLE-7
MOLECULAR DOCKING BINDING ENERGY OF 2-METHYL-1,4-NAPHTHOQUINONE

Protein ID	Binding affinity (kcal/mol)	Residues involved between ligand and protein	H-bonding involved between ligand and protein
1M17	-7.2	LYS A:721, ASP A:831, LEU A:820, VAL A:702, ALA A:719	ASP A:831(3.80 Å)
1A52	-7.1	LEU A:525, LEU A:384,ILE A :424, MET A :421, HIS A:524, GLY A:521	HIS A:524(2.72 Å)
3D90	-6.6	LYS A:822, ARG A:766, PRO A:696, SER A:728, ILE A:699	SER A:728(2.76 Å)

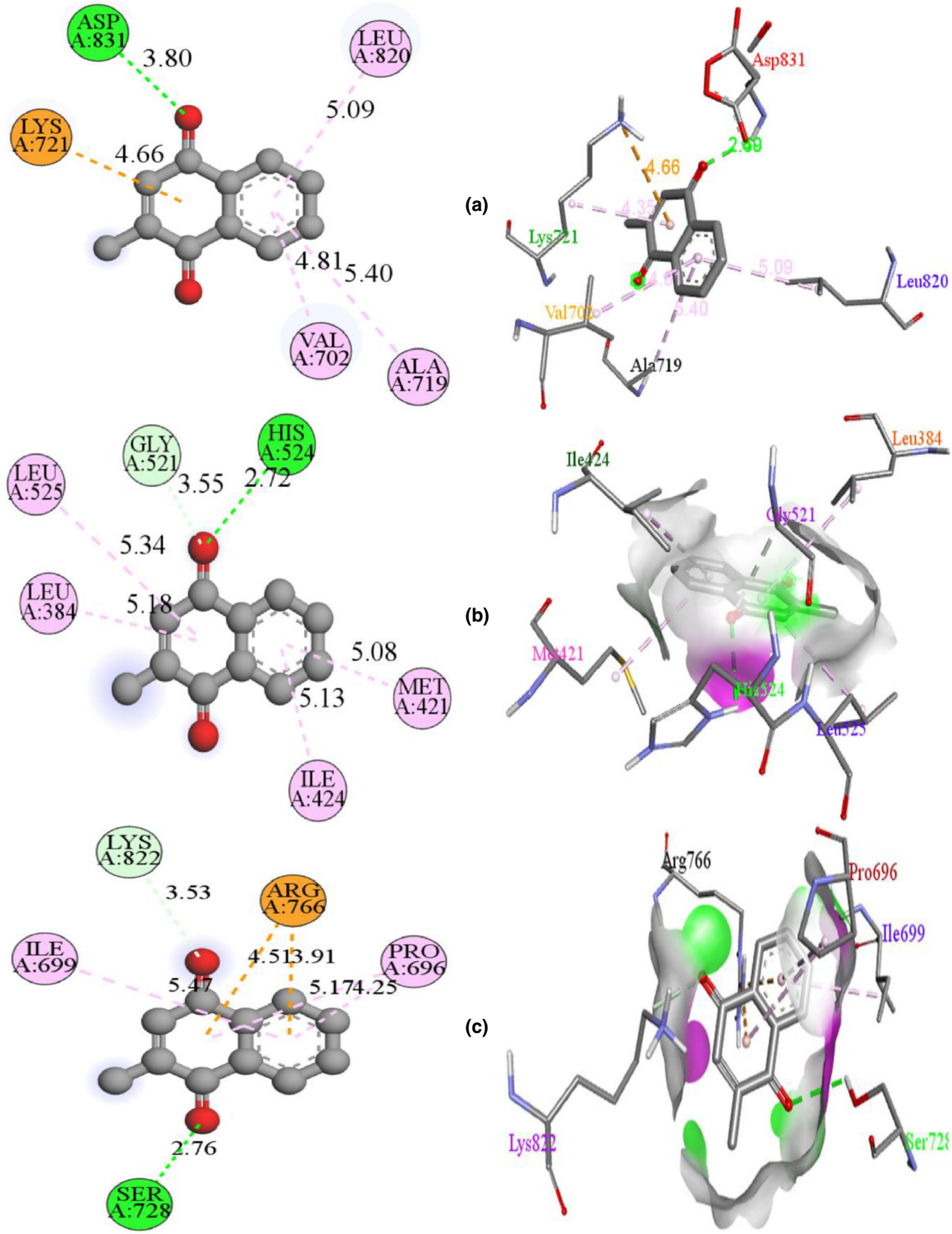

Fig. 8. Molecular docking of 2D and 3D interaction with H-bond of 2-methyl-1,4-naphthoquinone with PDB ID: (a) 1M17, (b) 1A52 and (c) 3D90

TABLE-8
PHARMACOKINETIC PREDICTION OF 2-METHYL-1,4-NAPHTHOQUINONE

ADMET properties		MNQ	Anastrozole
Absorption	CaCo-2 permeability (log Papp in 10^{-6} cm/s)	1.322	1.022
	Human intestinal absorption (%)	97.779	98.8
	Skin permeability (log Kp)	-2.346	-2.7
Distribution	VDss (human) (log L/kg)	0.094	-0.097
	Fraction unbound (human)	0.328	0.163
	BBB permeability (log BB)	0.408	-0.347
	CNS permeability (log PS)	-2.004	-2.736
Metabolism	CYP2D6 substrate	No	No
	CYP3A4 substrate	No	Yes
	CYP1A2 inhibitior	Yes	Yes
	CYP2C19 inhibitior	Yes	Yes
	CYP2C9 inhibitior	Yes	No
	CYP2D6 inhibitior	Yes	No
	CYP3A4 inhibitior	No	No
Excretion	Total clearance (log mL/min/kg)	0.223	1.525
	Renal OCT2 substrate	No	No
Toxicity	AMES toxicity test	Yes	Yes
	hERG I inhibitor	No	No
	hERG II inhibitor	No	No
	Oral rat acute toxicity (LD_{50}) (mol/kg)	1.696	2.363
	Oral rat chronic toxicity (log mg/kg_bw/day)	2.657	1.338
	Skin sensitization	Yes	No
	T. pyriformis toxicity (log ug/L)	0.718	1.69
	Minnow toxicity (log mM)	1.494	1.205
	Hepatotoxicity	Yes	Yes

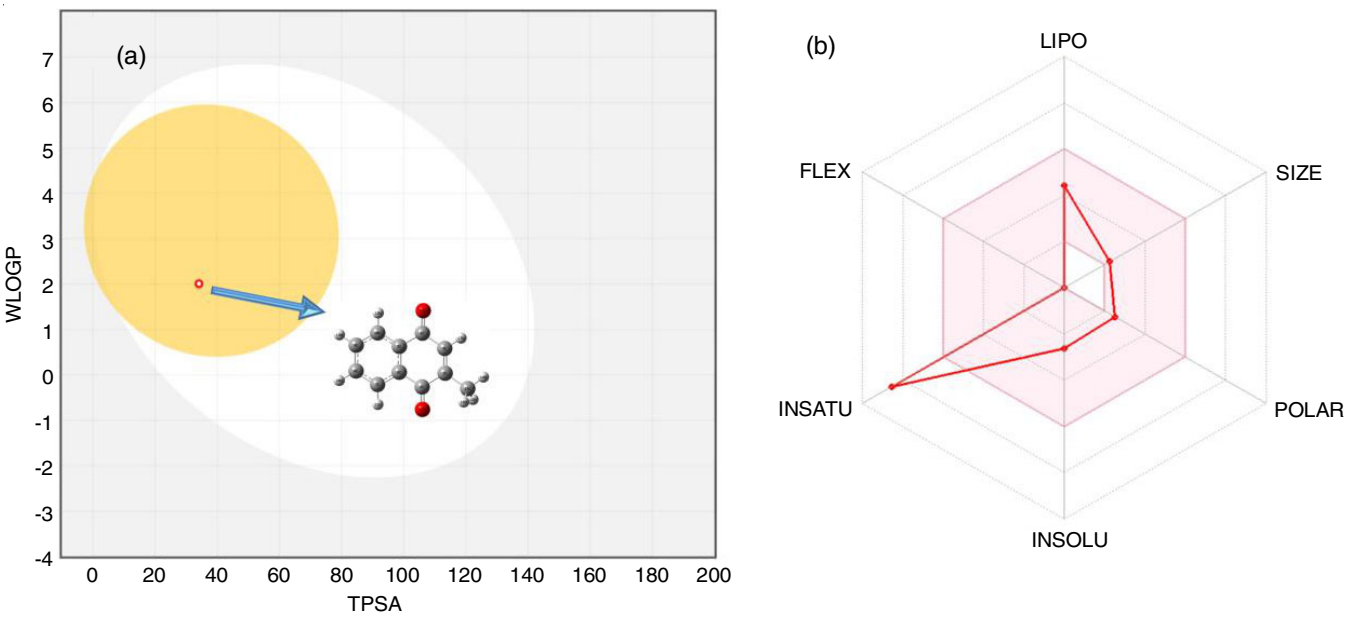

Fig. 9. (a) BOILED-Egg plot and (b) Radar plot of 2-methyl-1,4-naphthoquinone

be 0.09, indicating a relatively unsaturated structure. Lower saturation levels are often associated with increased aromaticity and planarity, which can influence bioavailability and binding interactions. Also, the ideal range for drug-like physico-chemical characteristics is represented by the pink-shaded area in the radar plots. Good ADMET behaviour depends on favourable properties such as appropriate lipophilicity, polarity and solubility parameters that fall within this pink zone. Conversely, the values outside this area indicate deviations from the optimal range, which may negatively affect bioavailability, distribution, or absorption. In this study, as illustrated in Fig. 11b, 2MNQ falls within the pink region, indicating a well-balanced and drug-like physicochemical profile. Lipophilicity values for iLOGP, XLOGP3, WLOGP, MLOGP and SILICOS-IT were 1.74, 2.20, 2.01, 1.20 and 2.72, respectively. Predicted water solubility values from ESOL, ALI and SILICOS-IT were –2.64, –2.55 and –3.42, respectively, indicating a solubility range from moderate to high. Based on the predicted pharmacokinetic and physico-chemical properties, 2MNQ appears to be a sufficiently safe and promising candidate for therapeutic applications.

Conclusion

The optimal geometries, harmonic vibrational wavenumbers and vibrational band intensities of 2-methyl-1,4-naphthoquinone (2MNQ) were determined using the DFT-B3LYP method with the standard 6-311 ++G(d,p) basis set. This level of computation was found to align well with experimental observations. The frequency assign-ments were further supported by potential energy distribution (PED) calculations. Furthermore, the electronic properties of molecule were analyzed and compared with the experimentally measured UV-Vis spectral values. Molecular docking results revealed that 2MNQ exhibits strong binding affinities to key breast cancer-related proteins 1M17, 1A52 and 3D9O with binding energies of –7.2, –7.1 and –6.6

kcal/mol, respectively. Finally, the physico-chemical and ADMET profiles of 2MNQ confirmed its drug-like behaviour. The compound complies with Lipinski's rule of five and demonstrates a favourable safety profile, supporting its potential as a therapeutic candidate.

CONFLICT OF INTEREST

The authors declare that there is no conflict of interests regarding the publication of this article.

REFERENCES

1. A. Ahmad, *Adv. Exp. Med. Biol.*, **1152**, 1 (2019); https://doi.org/10.1007/978-3-030-20301-6_1
2. A. Kutner, G. Brown and E. Kallay, *Int. J. Mol. Sci.*, **24**, 5621 (2023); https://doi.org/10.3390/ijms24065621
3. M.M. Rahman, M.R. Islam, S. Akash, S. Shohag, L. Ahmed, F.A. Supti, A. Rauf, A.S.M. Aljohani, W. Al Abdulmonem, A.A. Khalil, R. Sharma and M. Thiruvengadam, *Chem. Biol. Interact.*, **368**, 110198 (2022); https://doi.org/10.1016/j.cbi.2022.110198
4. I. Santra, S. Mukherjee, S.M. Haque and B. Ghosh, *Biotechnology and Conservation*, **33**, 375 (2023); https://doi.org/10.1007/978-981-19-9936-9_15
5. F.C. Demidoff, M.N. Rennó, C.D. Netto, *Stud. Natural Prod. Chem.*, **73**, 45 (2022); https://doi.org/10.1016/B978-0-323-91097-2.00016-9
6. J. Li, J. Wang and Z. Chen, *Mol. Cancer*, **24**, 13 (2025); https://doi.org/10.1186/s12943-024-02215-4
7. E.S. Ahmadi, A. Tajbakhsh, M. Iranshahy, J. Asili, N. Kretschmer, A. Shakeri and A. Sahebkar, *Mini Rev. Med. Chem.*, **20**, 2019 (2020); https://doi.org/10.2174/1389557520666200818212020
8. D.C. Joshi, A. Sharma, S. Prasad, K. Singh, M. Kumar, K. Sherawat, H.S. Tuli and M. Gupta, *Discov. Oncol.*, **15**, 342 (2024); https://doi.org/10.1007/s12672-024-01195-7
9. S. Khatun, R.P. Bhagat, S.A. Amin, T. Jha and S. Gayen, *Comput. Biol. Med.*, **175**, 108468 (2024); https://doi.org/10.1016/j.compbiomed.2024.108468
10. R. Rani, K. Sethi, S. Kumar, R.S. Varma and R. Kumar, *Chem. Biol. Drug Des.*, **100**, 786 (2022); https://doi.org/10.1111/cbdd.14122
11. K.R. Kavitha, Y.S. Mary and A. Fernandez, *Comput. Biol. Chem.*, **78**, 153 (2019); https://doi.org/10.1016/j.compbiolchem.2018.11.022
12. A.D. Becke, *Phys. Rev. A Gen. Phys.*, **38**, 3098 (1988); https://doi.org/10.1103/PhysRevA.38.3098
13. C. Lee, W. Yang and R.G. Parr, *Phys. Rev. B Condens. Matter*, **37**, 785 (1988); https://doi.org/10.1103/PhysRevB.37.785
14. M.J. Frisch, G.W. Trucks, H.B. Schlegel, G.E. Scuseria, M.A. Robb, J.R. Cheeseman, G. Scalmani, V. Barone, B. Mennucci, G.A. Petersson, H. Nakatsuji, M. Aricato, X. Li, H.P. Hratchian, A.F. Izmaylov, J. Bloino, G. Zheng, J.L. Sonnenberg, M. Hada, M. Ehara, K. Toyota, R. Fukuda, J. Hasegawa, M. Ishida, T. Nakajima, Y. Honda, O. Kitao, H. Nakai, T. Vreven Jr., J.A. Montgomery, J.E. Peralta, F. Ogliaro, M. Bearpark, J.J. Heyd, E. Brothers, K.N. Kudin, V.N. Staroverov, R. Kobayashi, J. Normand, K. Raghavachari, A. Rendell, J.C. Burant, S.S. Iyengar, J. Tomasi, M. Cossi, N. Rega, J.M. Millam, M. Klene, J.E. Knox, J.B. Cross, V. Bakken, C. Adamo, J. Jaramillo, R. Gomperts, R.E. Stratmann, O. Yazyev, A.J. Austin, R. Cammi, C. Pomelli, J.W. Ochterski, R.L. Martin, K. Morokuma, V.G. Zakrzewski, G.A. Voth, P. Salvador, J.J. Dannenberg, S. Dapprich, A.D. Daniels, Ö. Farkas, J.B. Foresman, J. Cioslowski, J.V. Ortiz and D.J. Fox, Gaussian 09, Revision A.1, Gaussian Inc., Wallingford CT (2009).
15. M.H. Jamroz, Vibrational Energy Distribution Analysis VEDA 4 Program, Warsaw (2004).
16. V. Balachandran, S. Lalitha and S. Rajeswari, *Indian J. Pure Appl. Phys.*, **52**, 799 (2014).
17. R. Dennington, T. Keith and J. Millam, GaussView, version 5, Semichem Inc., Shawnee Mission KS, (2009).
18. P. Tangyuenyongwatana and W. Gritsanapan, *Thai J. Pharm. Sci.*, **41**, 1 (2017).
19. O. Trott and A.J. Olson, *J. Comput. Chem.*, **31**, 455 (2010); https://doi.org/10.1002/jcc.21334
20. D.S. Biovia, BIOVIA Discovery Studio R2: A Comprehensive Predictive Science Application for the Life Sciences, San Diego, CA, USA (2017).
21. D.E.V. Pires, T.L. Blundell and D.B. Ascher, *J. Med. Chem.*, **58**, 4066 (2015); https://doi.org/10.1021/acs.jmedchem.5b00104
22. A. Daina, O. Michielin and V. Zoete, *Sci. Rep.*, **7**, 42717 (2017); https://doi.org/10.1038/srep42717
23. H. Nowell and J. Paul Attfield, *New J. Chem.*, **28**, 406 (2004); https://doi.org/10.1039/b306072a
24. S. Sumathi, S. Jeyavijayan, N. Karthik, A. Karthikeyan, P. Murugan and V.S. Kunjumol, *Asian J. Chem.*, **36**, 2025 (2024); https://doi.org/10.14233/ajchem.2024.32060
25. V.S. Kunjumol, S. Jeyavijayan, S. Sumathi and N. Karthik, *J. Mol. Recognit.*, **37**, e3074 (2024); https://doi.org/10.1002/jmr.3074
26. N. Karthik, S. Jeyavijayan and S. Sumathi, *Indian J. Biochem. Biophys.*, **61**, 204 (2024); https://doi.org/10.56042/ijbb.v61i4.8236
27. V.S. Kunjumol, S. Jeyavijayan, N. Karthik and S. Sumathi, *Spectrosc. Lett.*, **58**, 13 (2025); https://doi.org/10.1080/00387010.2024.2398025
28. N. Karthik, S. Jeyavijayan, M. Ramuthai, S. Sumathi and M.V. Kumar, *Indian J. Biochem. Biophys.*, **61**, 539 (2024); https://doi.org/10.56042/ijbb.v61i9.10826
29. J.S. kumar, N. Karthik, S. Sumathi, N.S. Jyothi, S. Saranya and S. Jeyavijayan, *Int. J. Quantum Chem.*, **124**, 1 (2024); https://doi.org/10.1002/qua.27509
30. A. Shiney, S. Jeyavijayan and M. Ramuthai, *J. Indian Chem. Soc.*, **101**, 101246 (2024); https://doi.org/10.1016/j.jics.2024.101246
31. T. Koopmans, *Physica*, **1**, 104 (1934); https://doi.org/10.1016/S0031-8914(34)90011-2
32. L.R. Domingo, M.J. Aurell, P. Pérez and R. Contreras, *Tetrahedron*, **58**, 4417 (2002); https://doi.org/10.1016/S0040-4020(02)00410-6
33. S. Sumathi, S. Jeyavijayan and N. Karthik, *J. Sci. Ind. Res.*, **83**, 1373 (2024); https://doi.org/10.56042/jsir.v83i12.8945
34. V.S. Kunjumol, S. Jeyavijayan, N. Karthik and S. Sumathi, *Indian J. Pure Appl. Phys.*, **62**, 576 (2024); https://doi.org/10.56042/ijpap.v62i7.7859
35. V.S. Kunjumol, N. Karthik, S. Sumathi and S. Jeyavijayan, *Indian J. Biochem. Biophys.*, **61**, 824 (2024); https://doi.org/10.56042/ijbb.v61i12.12427
36. S. Sukumaran, A. Zochedh, T.M. Viswanathan, A.B. Sultan and T. Kathiresan, *Polycycl. Aromat. Compd.*, **43**, 9443 (2023); https://doi.org/10.1080/10406638.2022.2164018
37. K.A.L. Azzam, *Resour.*, **325**, 14 (2023); https://doi.org/10.31643/2023/6445.13